actuators

MDPI

Article

Analysis of Rotor Vibration Characteristics in an Active Magnetic Suspension Flywheel Energy Storage System Considering the Unbalanced Magnetic Pull Force of the Motor

Lei Wang, Tielei Li * and Zhengyi Ren

College of Mechanical and Electrical Engineering, Harbin Engineering University, Harbin 150001, China; wanglei07@hrbeu.edu.cn (L.W.)
* Correspondence: litielei@hrbeu.edu.cn

Abstract

A flywheel energy storage system (FESS) is a device that employs a high-speed rotating flywheel for energy storage, where the motor is a core component enabling the energy conversion. Since the motor rotor is integrated onto the flywheel rotor (FR), when the FESS operates, the vortex motion of the FR causes misalignment between the motor rotor and stator, and the resulting unbalanced magnetic pull (UMP) will induce changes in the vibration characteristics of the FR. This paper presents a permanent magnet synchronous motor (PMSM) designed for a FESS and analyzes the variation pattern of the UMP induced by rotor eccentricity in this motor utilizing the finite element method. Furthermore, the UMP is equivalently modeled using the motor stiffness, and a dynamic model of an active magnetically suspended rigid flywheel rotor that considers the UMP in the motor is established. In this study, the motor position offset ratio β is defined to quantify the axial distance between the motor position and the FR mass center. This paper analyzes the variation law of the vibration characteristics of the FR with the magnitudes of the UMP and the motor position offset ratio β using numerical calculations. Finally, the correctness of the calculated results is verified using experimental testing. This investigation demonstrates that the value of UMP fluctuates as the rotor's rotation angle increases, while its average value exhibits a linear increasing trend with the growth in rotor eccentricity. As UMP and β increase, the first- and second-order critical speeds of FR exhibit a clear decreasing trend. Meanwhile, variations in these two factors also exert different influences on the vibration amplitude induced by the mass imbalance response of the FR. Therefore, when designing an active magnetically levitated flywheel energy storage system, the influence of motor parameters on the vibration characteristics of FR should be taken into consideration.

Keywords: flywheel rotor (FR); permanent magnet synchronous motor (PMSM); unbalanced magnetic pull (UMP); flywheel energy storage system (FESS); critical speed; mass imbalance response

Check for updates

Academic Editor: Moon Kyu Kwak

Received: 31 May 2026
Revised: 12 July 2026
Accepted: 21 July 2026
Published: 5 August 2026

Copyright: © 2026 by the authors. Licensee MDPI, Basel, Switzerland. This article is an open access article distributed under the terms and conditions of the Creative Commons Attribution (CC BY) license.

1. Introduction

A flywheel energy storage system (FESS) is an innovative physical energy storage device that employs a high-speed rotating flywheel to store energy and realizes the conversion between electrical energy and kinetic energy through a motor. It boasts the strengths of a large energy storage capacity density, high charging and discharging capacity, fast response speed, environmental friendliness, and long working life. In addition, it offers excellent practical engineering application value [1–3].

Motor design is a crucial task for the development of a FESS. Based on the application requirements of the FESS, the motor should be capable of both electric and power generation modes and possess high power, fast response speed, and high reliability. The motors commonly applied in flywheel energy storage systems include permanent magnet synchronous motors (PMSMs), induction motors (IMs), and switched reluctance motors (SRMs) [4–6]. In FESSs, the motor rotor is often integrated into the flywheel rotor shafting. When the flywheel rotor rotates, shafting vortex occurs in the motor rotor. This causes misalignment between the rotor and stator of the motor. The electromagnetic interaction between the motor rotor and stator not only generates torque but also produces a radial attractive force. When the rotor is concentric with the stator, this radial attractive force is balanced. However, when the rotor and stator are in a non-concentric state, unbalanced magnetic pull (UMP) will be generated [7–9]. During the operation of the FESS, the motor rotor is inevitably subjected to the action of UMP, which will further affect the vibration properties of the FR [10,11]. Therefore, when designing the motor for FESSs, it is necessary to investigate its operating performance and also consider the influence of UMP on the vibration characteristics of the FR. In recent years, many scholars have conducted extensive research on the design of flywheel energy storage system motors, the UMP in motors, and the vibration properties of motor rotors.

Numerous investigations on the performance of motors in FESSs have been reported. Liu et al. [12] achieved an improvement in the performance and a reduction in the loss of an outer rotor ironless brushless DC motor by optimizing its magnetic poles and windings. Sun et al. [13–15] proposed a cup-shaped winding permanent magnet synchronous motor (PMSM) applied to a large-capacity FESS that could effectively decrease the axial height of flywheel and achieve an increase in the efficiency as well as a reduction in power consumption of the FESS. Wang et al. [16] optimized the rotor structure of the permanent magnet synchronous motor in a FESS, achieving a reduction in harmonic current and temperature on the rotor, effectively avoiding irreversible demagnetization of the permanent magnet. Chen et al. [17] designed a composite rotor of a PMSM with high speed for an 200 kW/20,000 rpm uninterruptible power supply flywheel energy storage system. This composite rotor could suppress eddy current losses in rotor and solve the heat dissipation problem. Li et al. [18] conducted multi-objective optimization on the structural parameters of the high-speed surface-mounted permanent magnet synchronous motor (SMPSM) in a magnetically suspended flywheel energy storage system, thereby improving the efficiency of the SMPSM and reducing its weight and torque ripple. Jiang et al. [19] designed a dual three-phase stator winding structure and auxiliary teeth for the PMSM used in FESSs, ensuring the motor's fault tolerant operation under a series of winding open circuit faults, effectively reducing the current during winding short circuits, and thus improving the operational stability of motor.

During research on the vibration characteristics of the rotor, the bearing parameters, the frame support system, and the foundation excitation have important effects on the vibration characteristics of the rotor [20,21]. In addition, the unbalanced magnetic pull force of the motor has an important impact on the vibration characteristics of the rotor. Li et al. [22] proposed an analytical calculation model for the eccentricity air gap magnetic flux density in the slotted permanent magnet motor rotor that could quickly and accurately determine the corresponding magnetic field and unbalanced magnetic pull force under the condition of rotor eccentricity. Song et al. [23] adopted a FEM to study the UMP distribution of a motor rotor under different eccentricity conditions. The investigation revealed that the distributions of unbalanced magnetic pull force under static, dynamic, and mixed eccentricities were strip shaped, concentric and circular, and eccentric tooth shaped, respectively Zhang et al. [24] investigated the dynamic characteristics of the energy

storage flywheel rotor when there was initial static eccentricity in the induction motor rotor. The study suggested that the static eccentricity would change the displacement waveform of the rotor as well as the shape and position of the axis trajectory. Furthermore, the frequency components related to the stator rotating magnetic field appeared in the rotor vibration spectrum, and new resonance peaks appeared in the acceleration response of the rotor. Xu et al. [25] proposed an air gap length model considering static and dynamic eccentricity and determined the UMP solution method. Subsequently, they established a rotor dynamics model considering this UMP; they also studied the vibration responses of the rotor under large and small relative eccentricity conditions. Liu et al. [26] reported a rotor system dynamics model considering the mass eccentricity, position eccentricity, angular eccentricity, as well as transverse electromagnetic torque of PMSM rotor, and these researchers also studied the vibration response of the motor rotor. The research indicated that various eccentricities of the motor rotor, unbalanced magnetic pull force, and lateral electromagnetic torque would cause the radial and inclined vibration coupling of the motor rotor. Hao et al. [27] built a dynamic model of the electric spindle system and investigated the influence of factors such as internal motor parameters, rotor static eccentricity, and bearing parameters on the dynamic characteristics of the spindle rotor. It demonstrated that the variation in the static eccentricity of the rotor caused the amplitude curve to exhibit complex nonlinear phenomena. Dai et al. [28] researched the nonlinear dynamical characteristics of the PMSM rotor, revealing the affect patterns of the UMP and mass eccentricity excitation on rotor vibration properties. Michon et al. [29] conducted a study on the UMP of the rotor and stator in a large permanent magnet motor and the impact of this force on the bearing's load and lifespan. The results showed that the UMP had a pronounced effect on the lifespan of bearing. Feng et al. [30] proposed a semi-analytical method to describe the UMP force of a tilted eccentric rotor and its electromagnetic torque, established a rotor dynamics model for the spindle bearing unit, and also explored its dynamic displacement eccentric vibration response. The results demonstrated that the coupling effect of the UMP, mass unbalance force, as well as bearing force had a significant impact on the spindle bearing system.

Currently, although researchers have conducted relevant studies on the unbalanced magnetic pull (UMP) of motors in FESSs and the impact of this force on rotor vibration characteristics, there are relatively few investigations into the impact of motor UMP on the vibration characteristics of the FR in active magnetic-suspended flywheel energy storage systems. Therefore, this article first analyzes the characteristics of the UMP induced by rotor eccentricity in motor and then explores the effect of UMP in the motor on vibration characteristics of the rotor in an active magnetically levitated flywheel energy storage system.

The layout of this article is arranged as follows: Part 2 introduces the permanent magnet synchronous motor structure employed in the FESS and analyzes the variation rules of the unbalanced magnetic pull (UMP) under various rotor eccentricities in the motor using the finite element method. Furthermore, the unbalanced magnetic pull force (UMP) is equivalently treated. Part 3 constructs the dynamic model of an active magnetically suspended rigid flywheel rotor considering the UMP in the motor. Part 4 analyzes the influence of the UMP on the critical speed and mass imbalance response of the FR. Part 5 introduces the experimental platform and the test procedure and compares the theoretical values with measured data. Part 6 presents the conclusions of this paper.

2. Analysis of Unbalanced Magnetic Pull Force Caused by Rotor Eccentricity in a Permanent Magnet Synchronous Motor

2.1. Problem Description and Analysis

Permanent magnet synchronous motors (PMSMs) exhibit the strengths of fast response and high efficiency, and these motors are highly suitable as an energy conversion component for FESSs. Figure 1 displays the diagram of the radial cross-section structure for the PMSM studied in this work. The stator of this motor is a six-slot structure, and the stator winding adopts a three-phase winding form with a star connection. The permanent magnet rotor of this motor is composed of four-pole permanent magnet patches, and a stainless steel sheath is employed to secure the strength of the rotor structure. The permanent magnet patches are radially magnetized rubidium iron boron permanent magnets. The magnetic poles on the outer diameter surface of each permanent magnet patch are shown in Figure 1, where N represents the positive pole and S represents the negative pole. In addition, when there is a radial eccentricity r_d between the rotor center O_d and the stator center O, the gap width between the motor rotor and stator will exhibit an uneven distribution. A magnetic circuit is formed between the rotor and the stator of the motor, and the magnetic flux density in this circuit is related to the width of the air gap. On the side with a smaller gap width (in the positive direction of r_d), the magnetic field density in the air gap is higher, which results in a greater attraction between the motor stator and the rotor; conversely, on the side with a larger gap width (in the opposite direction of r_d), the attraction between the motor stator and the rotor is smaller. Therefore, when the motor rotor has an eccentricity r_d, an unbalanced magnetic pull force F_d in the same direction as r_d will be generated in the motor. The basic structural parameters for this motor are presented in Table 1.

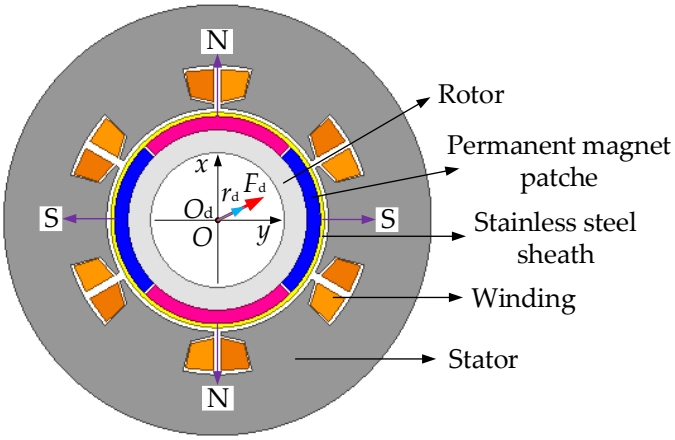


Figure 1. Planar structure diagram of this permanent magnet synchronous motor.

Table 1. Basic structure parameters of this PMSM.

Parameters	Values
Inner/outer radius of rotor	25 mm/33.5 mm
Inner/outer radius of the permanent magnet	33.5 mm/38.5 mm
Inner/outer radius of stator	42 mm/80 mm
Axial dimensions of motor	82 mm
Remanent magnetic strength of the permanent magnet	1.17 T
The coercivity resistance of the permanent magnet	880 kA/m

During operation of the FESS, the flywheel rotor (FR) will generate vortex due to the effect of the unbalanced mass. This causes the motor rotor integrated on the flywheel rotor to produce radial displacement, thereby generating unbalanced magnetic pull (UMP). This

will directly affect the vibration characteristics of the FR. In this paper, the flywheel rotor is supported by electromagnetic bearings, which have lower support stiffness compared to rolling bearings and sliding bearings. The impact of the UMP on the vibration characteristics of the FR will be more prominent, thus it is necessary to explore the influence of this UMP in the motor on the vibration characteristics of the active magnetically suspended flywheel rotor.

This work first uses the finite element method (FEM) to analyze the variation rules of the UMP rotor eccentricity and, on this basis, establishes a dynamic model of an active magnetically levitated flywheel rotor considering the UMP. Then, the influence rules of the magnitude and position of UMP in the motor on the vibration properties of FR are analyzed.

2.2. Analysis of Unbalanced Magnetic Pull Force in the Motor Based on the Finite Element Method

During the calculation of the magnetic field of the PMSM, it is assumed that the rotor axis of the motor is parallel to its stator axis, and the end effects are ignored. The magnetic field of the PMSM (as shown in Figure 1) is solved using the two-dimensional FEM, and the resulting magnetic field cloud map is presented in Figure 2. Figure 2a demonstrates the magnetic flux line distribution for this PMSM, from which it can be seen that no leakage phenomenon appears. Figure 2b exhibits the corresponding magnetic flux cloud map, from which it can be noticed that the maximum magnetic flux appears at the boundary between each permanent magnet on the rotor. The magnetic field distribution for this permanent magnet synchronous motor is reasonable, indicating that the structure design of this motor is reasonable.

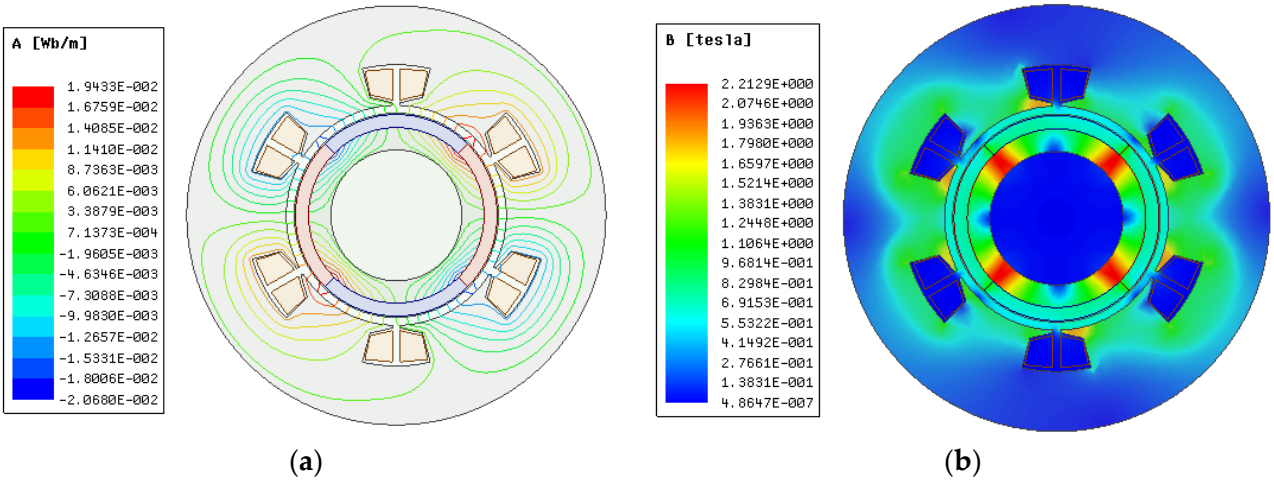


Figure 2. Magnetic field distribution diagram of the PMSM: (**a**) Magnetic field line distribution; (**b**) magnetic flux distribution cloud map.

According to the radial magnetic flux density in the air gap between the rotor and stator of the motor, the radial force acting on the motor rotor, namely the unbalanced magnetic pull (UMP), can be obtained. Set the eccentricity of the motor rotor to 0.1 mm and 0.2 mm, respectively. Under these different eccentricity conditions, set the maximum amplitude of the motor winding current to 0 A, 50 A, and 100 A, respectively. Then, the variation curves of the motor UMP with the rotor rotation angle are obtained, as presented in Figure 3a.

As can be observed in Figure 3a, when the rotor eccentricity r_d is 0.1 mm and 0.2 mm, the UMP of motor fluctuates around 22.5 N and 45 N, respectively. That is, the motor UMP exhibits fluctuating changes with the increase in the rotor rotation angle. Thus, the magnitude of the UMP is mainly affected by the rotor eccentricity r_d. When the winding current I_m is 50 A and r_d is 0.1 and 0.2 mm, respectively, the ratios of the fluctuation

amplitudes of UMP to their average values both are about 5%. When I_m is 100 A and r_d is 0.1 and 0.2 mm, respectively, this ratio is about 10%. This means that the ratio of the fluctuation amplitude of the UMP to its average value is related to the winding current I_m. The larger I_m is, the higher this ratio will be. When I_m is small, the discrepancy between the fluctuation amplitude of the UMP and its average value is relatively small. Therefore, when the winding current of stator is small, the average value of the motor's UMP that varies with the rotation angle of rotor can be utilized to evaluate the unbalanced magnetic pull force in the motor. The motor studied in this work belongs to the case where the winding current is relatively small; thus, the variation in its UMP with the eccentricity of the motor rotor can be obtained, as illustrated in Figure 3b.

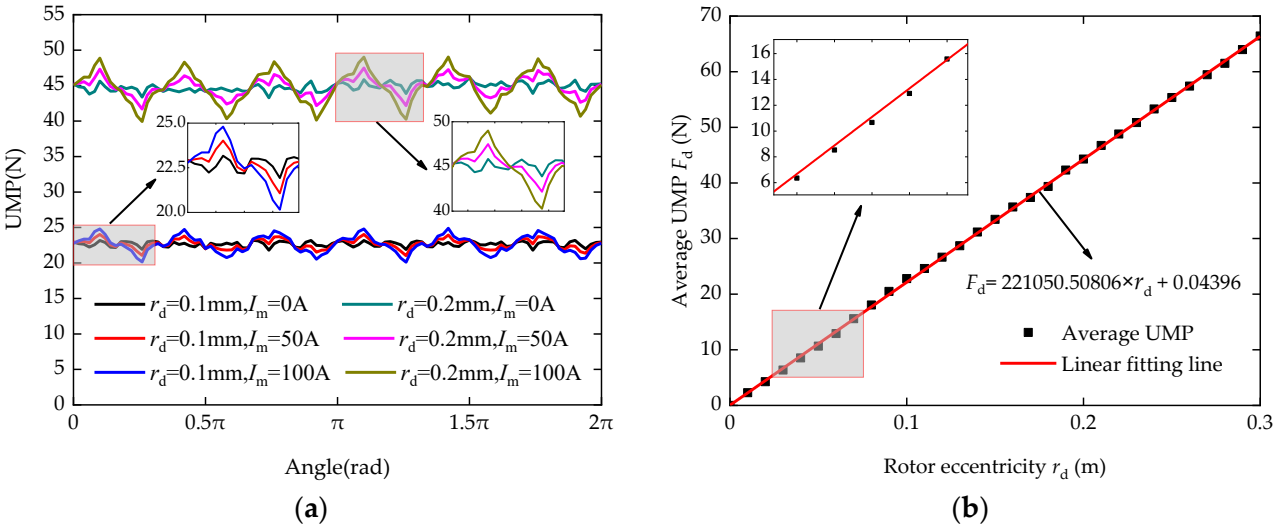


Figure 3. The variation curve of the UMP of motor rotor: (**a**) The variation in UMP with the rotation angle of the rotor; (**b**) the variation in UMP with rotor offset.

Usually, the unilateral air gap of the radial magnetic bearing is small; in this study, it is set at 0.3 mm. Therefore, the range of the rotor eccentricity r_d is determined to be 0–0.3 mm. Figure 3b demonstrates the values of the UMP under different r_d as well as the curve (red line) obtained by performing linear fitting on the values of UMP. Additionally, the linear fitting expression is given in this figure. In addition, its fitting parameter R-Square (COD) is 0.99979, which is close to 1, indicating a good linear fit. From this figure, it can be found that the UMP of motor has a linear increasing trend as the rotor eccentricity increases, which has a good consistency with the fitted straight line. Therefore, the UMP of motor can be linearized, and it can be equivalent to the product of the motor stiffness and eccentricity. Since the constant term of the fitting line expression shown in Figure 3b is very small, this constant term can be omitted.

By rounding the slope of the fitting line, the unbalanced magnetic pull force UMP of motor can be written as follows:

$$F_d = k_d \cdot r_d \quad (1)$$

where k_d is motor stiffness. Based on the linear fitting expression given in Figure 3b, the stiffness parameter k_d of the PMSM introduced in this paper is 2.2105×10^5 N/m.

The smaller the amplitude of the stator winding current is, the closer the unbalanced magnetic pull force of the motor at each rotor angle is to its average value, that is, the smaller the error between the motor stiffness and the motor UMP. Therefore, when the current of the motor stator winding is smaller, the usability of the motor stiffness obtained in this paper is better. This paper uses the motor stiffness k_d to measure the magnitude of the UMP of motor and, based on this, conducts the dynamic modeling of the flywheel rotor.

3. Dynamic Model Considering the Unbalanced Magnetic Pull Force of Motor

As the rotational speed increases, the flywheel rotor (FR) will transition from a rigid mode to an elastic mode. The supporting stiffness of the magnetic levitation bearing is relatively lower compared to other types of bearings. In addition, electromagnetic bearing is suitable for achieving suspension and control of rigid rotor, and the rotational inertia and mass of the FR are both relatively large. Usually, the FR in an active magnetic levitation flywheel energy storage system is designed as a rigid rotor (that is, the FR is in a rigid mode within the design speed). Therefore, during the process of conducting dynamic modeling, the flywheel rotor is assumed to be a rigid rotor.

In the active magnetically levitated flywheel energy storage system, the axial movement of the FR is constrained by the axial bearing, and when the FR tilts, it will rotate around the center of the axial bearing rotor. Therefore, a fixed coordinate system O-xyz is built with the geometric center O of the axial bearing rotor under the initial equilibrium position of FR as the origin. The corresponding force analysis diagram of the FR obtained is given in Figure 4. This figure presents the force distribution of the FR and its relevant structural parameters. Here, O is the geometric center of the axial bearing rotor; M denotes the mass center of the FR without considering the unbalanced mass; O_d is the geometric center of motor rotor; l_a and l_b denote the distances for the upper and lower radial bearings relative to the FR mass center, respectively; l_z and l_d are the distances of the axial bearing and motor relative to FR mass center, respectively; ω denotes the angular velocity of FR (rad/s); and θ_x, θ_y and M_{xz}, M_{yz} represent the rotation angle and torque of FR with respect to the y- and x-axis, respectively. Additionally, considering that the tilt rotation angle θ of FR is relatively minor in magnitude, let $\sin\theta \approx \theta$, $\cos\theta \approx 1$.

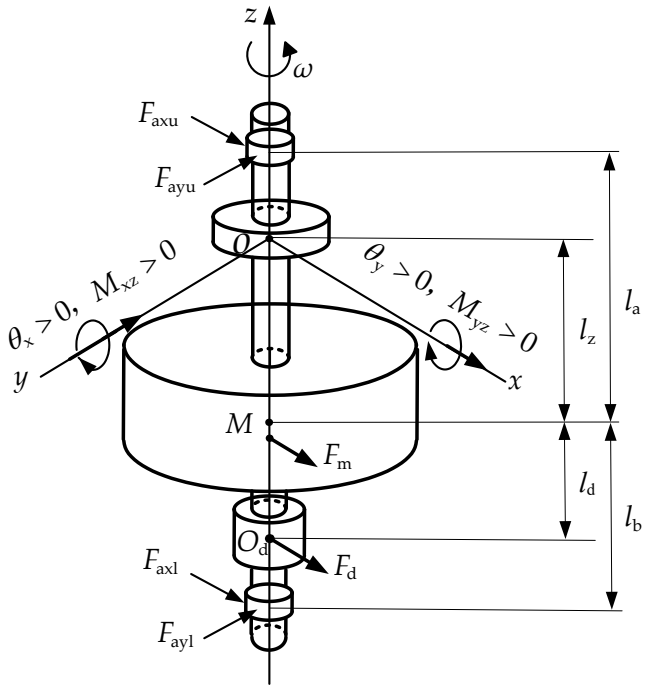


Figure 4. Diagram of force analysis of the flywheel rotor.

As demonstrated in Figure 4, the flywheel rotor is subjected to the support forces (F_{axu}, F_{ayu}, F_{axl}, F_{ayl}) from the radial magnetic bearing, the mass unbalance force F_m, the radial bearing support moments (M_{ax}, M_{ay}), and the mass unbalance moments (M_{mx}, M_{my}). In addition, the rotational vortex of the FR will cause radial movement of the center O_d of motor rotor, which leads to an uneven air gap and magnetic field distribution between the

stator and rotor. This causes an unbalanced radial force on the motor rotor (namely, the unbalanced magnetic pull force F_d) and unbalanced magnetic pulling force torque (M_{dx}, M_{dy}), which will directly affect the vibration characteristics of the flywheel rotor.

The supporting force F_a exerted by the radial active magnetic suspension bearing on the flywheel rotor can be expressed using equivalent dynamic stiffness k_a and damping c_a. Here, the parameters of k_a and c_a for the active magnetic suspension bearing with PID controller can be stated as follows [31]:

$$\begin{cases} k_a = \frac{-k_i K_s K_a}{(1+T_s{}^2\omega^2)(1+T_a{}^2\omega^2)}[(1-T_sT_a\omega^2)(K_p+\frac{K_dT_d\omega^2}{1+T_d{}^2\omega^2})+\omega(T_s+T_a)(-\frac{K_i}{\omega}+\frac{K_d\omega}{1+T_d{}^2\omega^2})]-k_x \\ c_a = \frac{-k_i K_s K_a}{\omega(1+T_s{}^2\omega^2)(1+T_a{}^2\omega^2)}[(1-T_sT_a\omega^2)(-\frac{K_i}{\omega}+\frac{K_d\omega}{1+T_d{}^2\omega^2})-\omega(T_s+T_a)(K_p+\frac{K_dT_d\omega^2}{1+T_d{}^2\omega^2})] \end{cases} \quad (2)$$

where k_i and k_x denote the stiffness coefficients of the current and displacement of the electromagnetic force, respectively; K_p, K_i, and K_d denote the proportionality coefficient, integral coefficient, and differential coefficient, respectively; K_s is displacement sensor coefficient; K_a is the power amplifier coefficient; T_s, T_a, and T_d denote the time constants of the displacement sensor, power amplifier, and differential unit, respectively; and ω denotes the angular frequency of FR (rad/s).

Then, the forces exerted by the radial magnetic bearing on FR in x and y directions (F_{ax} and F_{ay}), as well as the moments generated by the radial magnetic bearing mounted on FR relative to the y- and x-axes (M_{ax} and M_{ay}), can be stated as follows:

$$\begin{cases} F_{ax} = -k_{au}\cdot x_u(t) - c_{au}\cdot\dot{x}_u(t) - k_{al}\cdot x_l(t) - c_{al}\cdot\dot{x}_l(t) \\ F_{ay} = -k_{au}\cdot y_u(t) - c_{au}\cdot\dot{y}_u(t) - k_{al}\cdot y_l(t) - c_{al}\cdot\dot{y}_l(t) \\ M_{ax} = -l_a\cdot(k_{au}\cdot x_u(t) + c_{au}\cdot\dot{x}_u(t)) + l_b\cdot(k_{al}\cdot x_l(t) + c_{al}\cdot\dot{x}_l(t)) \\ M_{ay} = -l_a\cdot(k_{au}\cdot y_u(t) + c_{au}\cdot\dot{y}_u(t)) + l_b\cdot(k_{al}\cdot y_l(t) + c_{al}\cdot\dot{y}_l(t)) \end{cases} \quad (3)$$

where $x_u(t)$ and $y_u(t)$ denote the position of the upper radial bearing rotor, which can be written as $x_u(t) = x(t) + (l_a - l_z)\cdot\theta_x(t)$ and $y_u(t) = y(t) + (l_a - l_z)\cdot\theta_y(t)$, respectively; $x_l(t)$ and $y_l(t)$ denote the position of the lower radial bearing rotor, which can be written as $x_l(t) = x(t) - (l_b + l_z)\cdot\theta_x(t)$ and $y_l(t) = y(t) - (l_b + l_z)\cdot\theta_y(t)$, respectively; k_{au} and c_{au} are the equivalent stiffness and damping of the upper radial bearing; k_{al} and c_{al} are the equivalent stiffness and damping of the lower radial bearing; and $x(t)$ and $y(t)$ denote the position of axial bearing rotor.

According to the expression of the motor unbalance magnetic pull force shown in Equation (1), the unbalanced magnetic pull (UMP) force acting on flywheel rotor in the directions of x and y (F_{dx} and F_{dy}), as well as the torque generated by the UMP on FR relative to the y- and x-axes (M_{dx} and M_{dy}), can be respectively stated as follows:

$$\begin{cases} F_{dx} = k_d\cdot(x(t) - (l_z + l_d)\cdot\theta_x(t)) \\ F_{dy} = k_d\cdot(y(t) - (l_z + l_d)\cdot\theta_y(t)) \\ M_{dx} = -k_d\cdot(x(t) - (l_z + l_d)\cdot\theta_x(t))\cdot l_d \\ M_{dy} = -k_d\cdot(y(t) - (l_z + l_d)\cdot\theta_y(t))\cdot l_d \end{cases} \quad (4)$$

where k_d represents the motor stiffness, and l_d represents the distance between the motor and FR mass center.

In addition, due to the presence of the unbalanced mass on flywheel rotor, a mass imbalance force will be generated during its rotation, and the magnitude of this force varies proportionally with the square of rotating speed. The mass imbalance force (F_{mx} and F_{my}) acting on FR along the x and y directions, as well as the torque (M_{mx}, M_{my}) generated by

this mass imbalance force around the y- and x-axes on the flywheel rotor, can be expressed as follows:

$$\begin{cases} F_{mx} = U_m(at+\omega_0)^2\cos(0.5at^2+\omega_0 t+\alpha_0) \\ F_{my} = U_m(at+\omega_0)^2\sin(0.5at^2+\omega_0 t+\alpha_0) \\ M_{mx} = -U_m l_m(at+\omega_0)^2\cos(0.5at^2+\omega_0 t+\alpha_0) \\ M_{my} = -U_m l_m(at+\omega_0)^2\sin(0.5at^2+\omega_0 t+\alpha_0) \end{cases} \tag{5}$$

where U_m represents the mass imbalance quantity; l_m denotes the axial spacing between the unbalanced mass and FR mass center M; and α_0, ω_0, and a are the initial rotation angle, initial angular velocity, and angular acceleration of the FR, respectively.

Based on Newtonian vector mechanics and the theorem of angular momentum and by combining Equations (2)–(5), the dynamic mathematical model of the active magnetic levitation rigid flywheel rotor considering the unbalanced magnetic pull (UMP) of the motor can be acquired as follows:

$$\begin{bmatrix} m & & -ml_\mathrm{z} & \\ & m & & -ml_\mathrm{z} \\ & & J_\mathrm{d}+ml_\mathrm{z}^2 & \\ & & & J_\mathrm{d}+ml_\mathrm{z}^2 \end{bmatrix}\begin{bmatrix} \ddot{x}(t) \\ \ddot{y}(t) \\ \ddot{\theta}_\mathrm{x}(t) \\ \ddot{\theta}_\mathrm{y}(t) \end{bmatrix} + \begin{bmatrix} A & & C & \\ & A & & C \\ B & & D & J_\mathrm{p}(at+\omega_0)^2 \\ & B & -J_\mathrm{p}(at+\omega_0)^2 & D \end{bmatrix}\begin{bmatrix} \dot{x}(t) \\ \dot{y}(t) \\ \dot{\theta}_\mathrm{x}(t) \\ \dot{\theta}_\mathrm{y}(t) \end{bmatrix} + \begin{bmatrix} E & & G & \\ & E & & G \\ F & & H & \\ & F & & H \end{bmatrix}\begin{bmatrix} x(t) \\ y(t) \\ \theta_\mathrm{x}(t) \\ \theta_\mathrm{y}(t) \end{bmatrix} = \begin{bmatrix} U_\mathrm{m}((at+\omega_0)^2\cos(0.5at^2+\omega_0 t+\alpha_0)) \\ U_\mathrm{m}((at+\omega_0)^2\sin(0.5at^2+\omega_0 t+\alpha_0)) \\ -U_\mathrm{m}l_\mathrm{m}((at+\omega_0)^2\cos(0.5at^2+\omega_0 t+\alpha_0)) \\ -U_\mathrm{m}l_\mathrm{m}((at+\omega_0)^2\sin(0.5at^2+\omega_0 t+\alpha_0)) \end{bmatrix} \tag{6}$$

where $A = c_\mathrm{au} + c_\mathrm{al}$; $B = c_\mathrm{au}l_\mathrm{a} - c_\mathrm{al}l_\mathrm{b}$; $C = c_\mathrm{au}(l_\mathrm{a} - l_\mathrm{z}) - c_\mathrm{al}(l_\mathrm{b} + l_\mathrm{z})$;

$D = c_\mathrm{au}l_\mathrm{a}(l_\mathrm{a} - l_\mathrm{z}) + c_\mathrm{al}l_\mathrm{b}(l_\mathrm{b} + l_\mathrm{z})$; $E = k_\mathrm{au} + k_\mathrm{al} - k_\mathrm{d}$; $F = k_\mathrm{au}l_\mathrm{a} - k_\mathrm{al}l_\mathrm{b} + k_\mathrm{d}l_\mathrm{d}$;

$G = k_\mathrm{au}(l_\mathrm{a} - l_\mathrm{z}) - k_\mathrm{al}(l_\mathrm{b} + l_\mathrm{z}) + k_\mathrm{d}(l_\mathrm{d} + l_\mathrm{z})$; and $H = k_\mathrm{au}l_\mathrm{a}(l_\mathrm{a} - l_\mathrm{z}) + k_\mathrm{al}l_\mathrm{b}(l_\mathrm{b} + l_\mathrm{z}) - k_\mathrm{d}(l_\mathrm{d} + l_\mathrm{z})l_\mathrm{d}$.

Furthermore, J_d is the equatorial moment of inertia of the flywheel rotor, and J_p is the polar moment of inertia of the flywheel rotor.

The dynamic model as shown in Equation (6) is appropriate for solving the vibration characteristic parameters of the FR under the rigid body mode. This paper utilizes this dynamic model to analyze the influence rule of the UMP on the vibration characteristics of the active magnetic levitation rigid flywheel rotor.

4. The Influence of Unbalanced Magnetic Pull Force of Motor on the Dynamic Characteristics of Active Magnetic Suspension Flywheel Rotor

The magnitude of the motor unbalanced magnetic pull (UMP) and its acting location will affect the force state of the flywheel rotor (FR), thereby altering the vibration properties of the active magnetically levitated flywheel rotor. The critical speed and mass imbalance response are important manifestations of the vibration characteristics of flywheel rotor. Therefore, this section explores the effect of the magnitude of motor UMP and its acting location on the critical speed and mass imbalance response of FR employing the numerical computation method.

4.1. Numerical Solution and Analysis of the Vibration Characteristic Parameters of FR

The structural and physical parameters for the FR are presented in Table 2. Additionally, the parameters for radial active magnetic bearing are listed in Table 3. Substitute these parameters into the dynamics model as shown in Equation (6), and solve this model using the fourth-order Runge–Kutta numerical method. Here, the motor stiffness k_d represents the magnitude of the UMP in motor, and the motor position l_d (namely, the axial distance between the motor and FR mass center) represents the location where the UMP acts. By

adjusting the parameters of k_d and l_d, the variation curve of the vibration amplitude of FR with speed can be obtained based on different UMP values and their acting positions. Here, the initial angular velocity ω_0 = 0.1 rad/s and angular acceleration a = 3 rad/s^2 are determined in the solving process.

Table 2. Structural and physical parameters of FR.

Parameters	Values
Mass of FR (m)	56 kg
Imbalance of FR (U_m)	8.9152×10^{-5} kg·m
Polar rotational inertia of FR (J_p)	0.93 kg·m^2
Equatorial rotational inertia of FR (J_d)	1.14 kg·m^2
Distance between the upper radial bearing and FR mass center (l_a)	0.282 m
Distance between the axial bearing and FR mass center (l_z)	0.145 m
Axial distance between the unbalanced mass and FR mass center (l_m)	0.08 m
Distance between the lower radial bearing and FR mass center (l_b)	0.273 m

Table 3. Parameters of the radial active magnetic bearing.

Parameters	Values
Current stiffness coefficient of electromagnetic force (k_i)	−252.8 N/A
Displacement stiffness coefficient of electromagnetic force (k_x)	2.1×10^6 N/m
Power amplifier coefficient (K_a)	0.5 A/V
Displacement sensor coefficient (K_s)	10,000 V/m
Time constant of power amplifier (T_a)	1×10^{-4}
Time constant of displacement sensor (T_s)	1×10^{-4}
Time constant of differential element (T_d)	1×10^{-4}
Proportionality coefficient (K_p)	2.05
Integral coefficient (K_i)	5×10^{-5}
Differential coefficient (K_d)	5×10^{-4}

When the stiffness k_d of the motor and its position l_d are 0 N/m and 0 m, 2.5×10^5 N/m and 0 m, and 2.5×10^5 N/m and 0.2 m, separately, the obtained curves of the FR's vibration amplitude versus the speed at the radial bearing positions are presented in Figure 5a,b. Figure 5a exhibits the amplitude curves of the FR at the position of its upper radial bearing, and Figure 5b demonstrates the amplitude curves at the lower radial bearing position.

From Figure 5a,b, it can be found that as the speed increases, there are two peaks in the amplitude curves of FR under its upper and lower radial bearing positions. The speeds at these two peak points stand for the first- and second-order critical speeds ω_{1c} and ω_{2c} of FR. As the motor is placed at the FR mass center (namely, l_d = 0 m), compared with the case where k_d = 0 N/m, when the motor stiffness k_d is 2.5×10^5 N/m, the ω_{1c} significantly decreases, and the vibration amplitude of FR at its radial bearing position significantly decreases under ω_{1c}. However, there is no significant change in ω_{2c} and its vibration amplitude under this speed. This indicates that the existence of motor stiffness (that is, the UMP in motor) has an obvious impact on the first critical speed ω_{1c} and that the vibration amplitude corresponds to this speed.

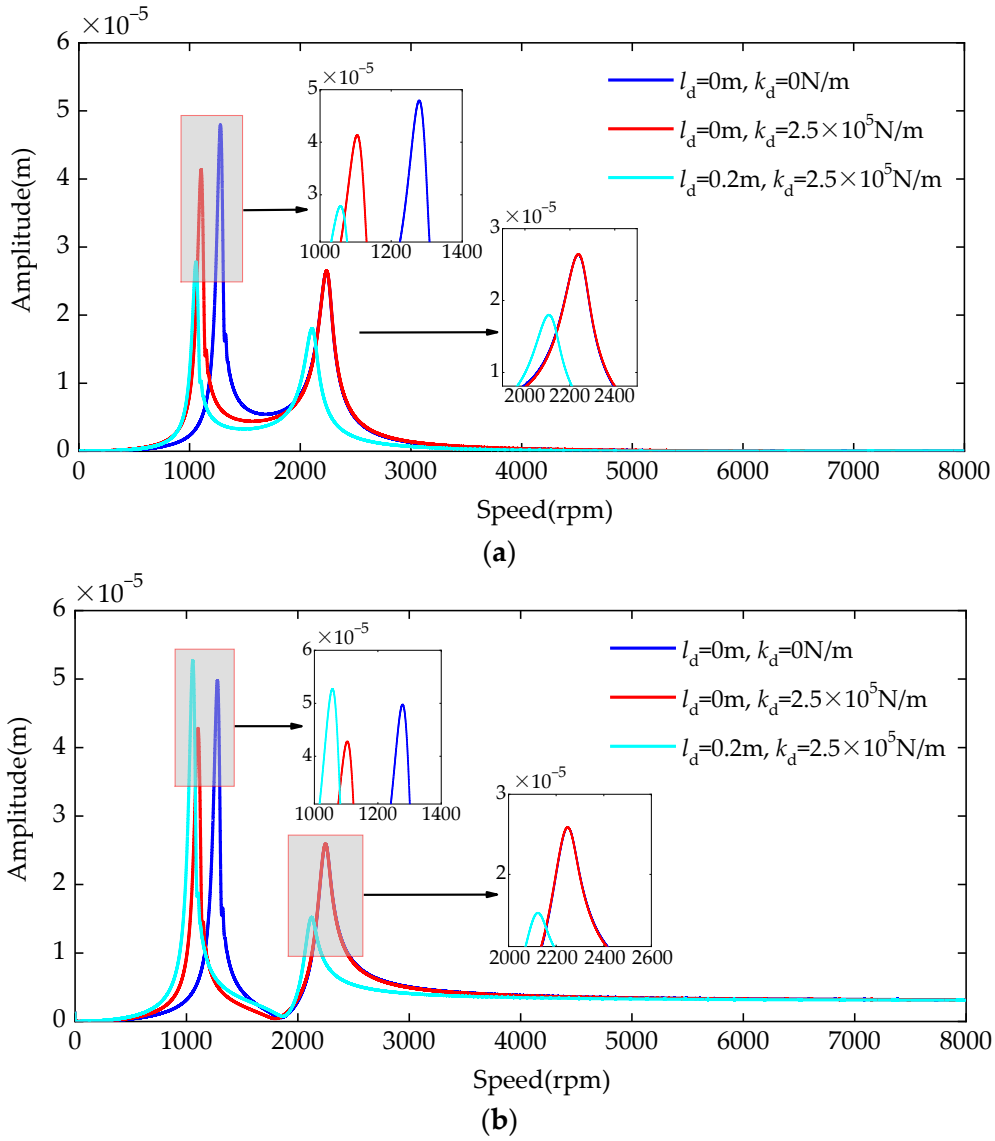


Figure 5. Under different motor stiffness k_d and position l_d, the variation curves of the flywheel rotor's vibration amplitude versus speed at the positions of radial bearing are presented: (**a**) Amplitude curves under the upper radial bearing position; (**b**) amplitude curves under the lower radial bearing position.

In addition, under the condition that the motor stiffness k_d is 2.5 × 10^5 N/m, compared to l_d = 0, when the motor position l_d is 0.2 m, the ω_{1c} and ω_{2c} of FR both decrease, and ω_{2c} exhibits a more obvious decreasing trend. Furthermore, below the first critical speed ω_{1c}, the corresponding vibration amplitude at the upper radial bearing significantly decreases, while that at the lower radial bearing significantly increases. Below the ω_{2c}, the vibration amplitudes of FR at the upper and lower radial bearings both obviously decrease. This demonstrates that the motor position l_d, which is the location where the UMP acts, has an obvious effect on critical speed of the FR and its vibration amplitude.

In addition, based on the displacement parameters (x, y) and tilt angle parameters (θ_x, θ_y) of the FR, the vibration modes (namely, the motion trajectory of the axis of FR) of the active magnetically levitated flywheel rotor at its first- and second-order critical speeds ω_{1c} and ω_{2c} can be obtained, as shown in Figure 6a,b. In this figure, the black straight line represents the axis of the FR, the red curve shows the motion trajectory of the FR at its upper radial bearing, the yellow curve denotes the motion trajectory at the mass center of

FR, the green curve indicates the motion trajectory of FR at the position of motor, and the blue curve represents the motion trajectory of FR at its lower radial bearing.

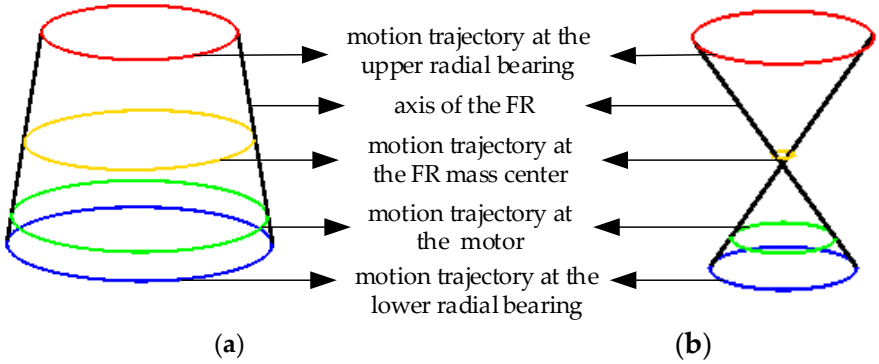


Figure 6. The vibration mode of FR: (**a**) Vibration mode at the first-order critical speed; (**b**) vibration mode at the second-order critical speed.

As indicated in Figure 6a, the FR exhibits a translational vibration mode below the critical speed ω_{1c}. Under this vibration mode, the critical speed of FR is closely related to the radial support force. However, the existence of motor UMP (namely, the motor stiffness k_d) will directly change the radial support force of the FR, thereby exerting a significant influence on ω_{1c}. In addition, Figure 6b shows that the FR presents a conical vibration mode at the critical speed ω_{2c}. Below this vibration mode, the critical speed of the FR is closely related to the supporting moment, while the changes of the UMP in motor and its acting position will directly affect the supporting moment on the flywheel rotor, thereby significantly influencing ω_{2c}.

In addition, under the translational vibration mode (this corresponds to the first-order critical speed), the variation in the magnitude of UMP and its acting location will alter the radial displacement and tilt angle of the FR; as these two factors increase, the vibration amplitudes at the positions of the upper and lower radial bearings exhibit the same or opposite tendencies. Under the conical vibration mode (this corresponds to the second-order critical speed), the change in the UMP will alter the inclination angle of the FR. At this time, as the inclination angle increases, the vibration amplitudes at the positions of the upper and lower radial bearings present the same trends.

4.2. The Influence of Motor Unbalanced Magnetic Pull Force on the Critical Rotation Speed of the Active Magnetic Suspension Flywheel Rotor

From the above analysis in Section 4.1, it can be concluded that the presence of the motor UMP will affect the vibration characteristics of the active magnetic suspension flywheel rotor. Critical speed is one of the significant features of rotor vibration. Hence, this section primarily explores the influence rules of the magnitude of motor UMP (characterized by motor stiffness k_d) and its acting position (characterized by motor position l_d) on the first- and second-order critical speeds (ω_{1c} and ω_{2c}) of the active magnetic suspension flywheel rotor.

In order to quantify the position of the motor on the flywheel rotor shaft system, the parameter of the motor position offset ratio β is defined. Its definition is as follows:

$$\beta = \frac{l_d}{l_b} \tag{7}$$

where l_d represents the distance between the motor and the mass center of FR, and l_b is the distance from the lower radial bearing to the mass center of FR. For the flywheel energy storage system studied in this paper, the motor is located between the mass center of FR

and the lower radial bearing. The range of parameter β is between 0 and 1, and the larger the β is, the greater the distance from the motor to the mass center of FR.

Under different motor position offset ratios β, the curves showing the variation in critical speed as motor stiffness k_d are presented in Figure 7. Here, Figure 7a,b demonstrate the curves of critical speeds ω_{1c} and ω_{2c} versus k_d when the β is 0, 0.177, 0.355, 0.532, and 0.709.

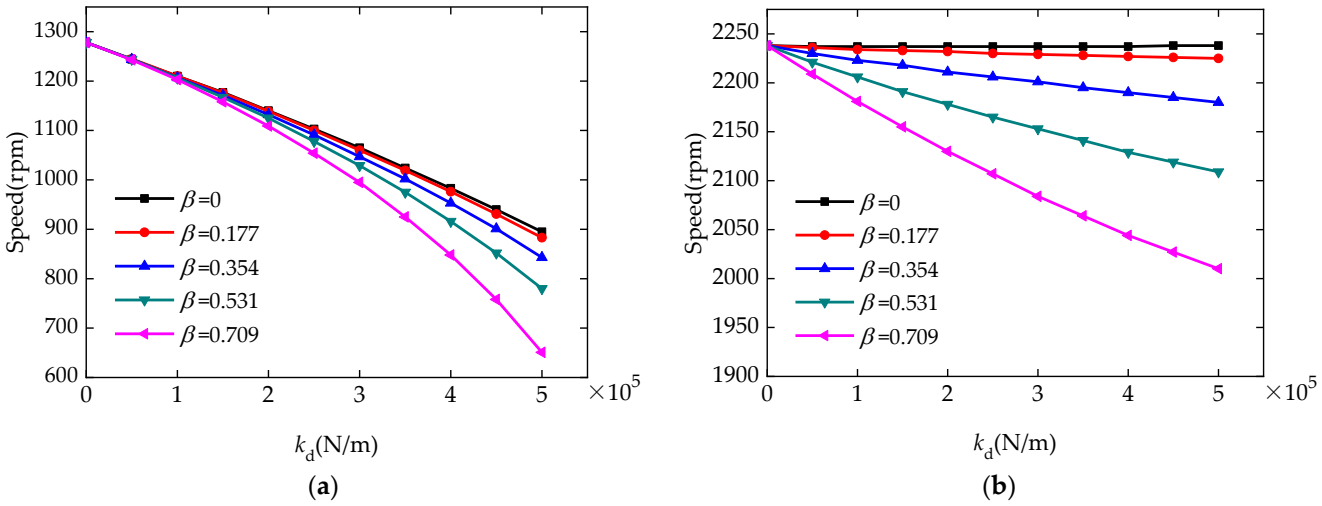


Figure 7. Curves of the critical speed of FR with k_d and β: (**a**) Variation curves of the first-order critical speed; (**b**) variation curves of the second-order critical speed.

As presented in Figure 7a, the changes in motor stiffness k_d and its position offset ratio β both have an obvious effect on the critical speed ω_{1c} of FR. With the increase in k_d and β, the ω_{1c} presents a declining tendency. It indicates that the rise of the UMP reduces the first critical speed of FR. In addition, as the axial distance l_d from the position of motor to the FR's mass center increases, the ω_{1c} also decreases. This is mainly because the direction of the UMP is opposite to that of the radial bearing support force. Specifically, compared to the stiffness of the radial bearing, the motor stiffness is a negative stiffness. The radial support stiffness of the FR will decrease as the motor stiffness increases. Moreover, at the critical speed ω_{1c}, the FR exhibits a translational mode (as shown in Figure 6a), and the critical speed under this vibration mode decreases with the decrease in its radial support stiffness. Thus, as the magnitude of the UMP increases, the first critical speed presents a decreasing trend. In addition, as the axial distance from the motor position and the FR mass center increases, the UMP torque acting on the FR increases, which leads to an increase in the inclined rotation angle of the FR. Due to the coupling between the radial motion and inclined rotation of the FR, ω_{1c} demonstrates a decreasing trend with the increase in l_d. In the case where β is 0, 0.355, and 0.709 and when $k_d = 2.5 \times 10^5$ N/m, the reduction in ω_{1c} is 13.7%, 14.6%, and 17.5%, respectively; when $k_d = 5 \times 10^5$ N/m, ω_{1c} decreases by 30%, 34%, and 49%, respectively. From this, it can be seen that the influence of motor stiffness k_d on the critical speed ω_{1c} is greater than that of the motor position offset ratio β on ω_{1c}.

Figure 7b shows that the changes in the motor stiffness k_d and its position offset ratio β both have a significant effect on the second critical speed ω_{2c}. When $\beta = 0$, the variation in k_d has no clear influence on ω_{2c}. However, when $\beta \neq 0$, ω_{2c} decreases as both k_d and β increase. This indicates that when the axial spacing l_d is 0, the increase in the motor's UMP produces no distinct impact on the second critical speed; however, as l_d and UMP increase, the ω_{2c} decreases. This is because the FR exhibits a conical vibration mode under the ω_{2c}, as shown in Figure 6b. In this mode, the critical speed for FR primarily depends on its supporting moment. When the axial spacing l_d is 0, the variation in the UMP shows no

significant impact on the supporting moment. However, this supporting moment decreases as l_d and UMP increase. This results in a reduction in the ω_{2c}. When $k_d = 2.5 \times 10^5$ N/m and β is 0.355 and 0.709, the corresponding critical speed ω_{2c} declines by 1.4% and 5.9%, respectively; furthermore, when $k_d = 5 \times 10^5$ N/m, and β is 0.355 and 0.709, ω_{2c} decreases by 2.6% and 10%, respectively. Thus, it can be seen that the effect of the motor stiffness k_d on the second critical speed ω_{2c} is smaller than that of the motor position offset ratio β on ω_{2c}.

From the above analysis, it can be concluded that the UMP in the motor and its acting position will significantly reduce the critical speed of the FR. In addition, the variation in the UMP exerts a more prominent impact on the first critical speed, while the change in its acting position produces a more distinct influence on the second critical speed. Therefore, during the process of an active magnetically levitated flywheel energy storage system design, in order to accurately determine the critical speed of the FR and its operating speed range, the effect of the UMP on the critical speed should be taken into account.

4.3. The Influence Rule of the Unbalanced Magnetic Pull Force of the Motor on the Mass Imbalance Response of the Active Magnetic Levitation Flywheel Rotor

The mass imbalance response is a vital manifestation of the operational stability of the flywheel rotor (FR), while the existence of the motor's UMP will change the force state of the FR, thereby affecting the mass imbalance response. As shown in the vibration amplitude curves illustrated in Figure 5 of Section 4.1, the presence of the UMP produces a significant effect on the vibration amplitude under critical speed. However, after the second critical speed, this vibration amplitude does not change significantly with the alteration in the motor stiffness k_d and the motor position l_d. Therefore, this part mainly discusses the change rules of the mass imbalance response for the FR under critical speed along with the variation in the UMP. Here, the motor position offset ratio β is adopted to quantify the axial position of this motor mounted on the FR, and $\beta = l_d/l_b$.

Under different β values at critical speeds, the calculated curves for vibration amplitude of FR at positions of its radial bearings versus k_d are presented in Figure 8a,b. Among them, under the critical speed ω_{1c}, when β is 0, 0.354, and 0.709, separately, the curves for the vibration amplitude (A_u^{1c}, A_l^{1c}) at the upper and lower radial bearing positions versus k_d are displayed in Figure 8a; meanwhile, under the critical speed ω_{2c}, the corresponding curves for vibration amplitude (A_u^{2c}, A_l^{2c}) are presented in Figure 8b.

Figure 8a reveals that the variations in motor stiffness k_d and its position offset ratio β both have a significant impact on the vibration amplitude for FR at the positions of its radial bearing below the first critical speed ω_{1c}. The vibration amplitude A_u^{1c} for FR at its upper radial bearing position decreases as k_d and β increase. However, the trend of its vibration amplitude A_l^{1c} at the lower radial bearing position with k_d is related to β. As β increases, the variation trend in A_l^{1c} with k_d changes from gradually decreasing to first increasing and then decreasing. This indicates that as the UMP and the axial distance l_d increase, the vibration amplitude at its upper radial bearing position decreases; however, its vibration amplitude at the lower radial bearing position shows different variation trends with the increase in l_d as the UMP changes. When l_d is small, the amplitude maintains a decreasing trend. However, as l_d increases, this evolves into a trend of first increasing and then decreasing. This is mainly because as the UMP and its axial distance l_d increase, the ω_{1c} decreases. This will lead to a significant reduction in its mass imbalance force at the speed of ω_{1c}, thereby causing a decrease in the vibration amplitude (A_u^{1c} and A_l^{1c}) under the position of the radial bearings. However, the increase in UMP and l_d will lead to a reduction in the radial support force imposed on FR, which will cause an increase in A_u^{1c} and A_l^{1c}. Additionally, the variation in the motor position will affect the support torque of FR. This will change the tilt angle of the FR; thus, the variation in the vibration amplitude

at the upper and lower radial bearing positions exhibits different trends. The variation pattern of the vibration amplitude at the position of radial bearings is a manifestation under the combined effects of various factors. Among them, in the case where β is 0, 0.355, and 0.709 and when $k_d = 2.5 \times 10^5$ N/m, A_u^{1c} decreases by 13.7%, 24.5%, and 33.1% respectively, and A_l^{1c} shows decreases of 14% and 2.6% as well as an increase of 7.4%, respectively. When $k_d = 5 \times 10^5$ N/m, A_u^{1c} decreases by 30.1%, 49.8%, and 82%, respectively, and the corresponding A_l^{1c} presents a decrease of 30.4%, 18.8%, and 29.9%, respectively. From this, it can be seen that both the motor stiffness k_d and its position offset ratio β have a distinct effect on the vibration amplitudes A_u^{1c} and A_l^{1c}.

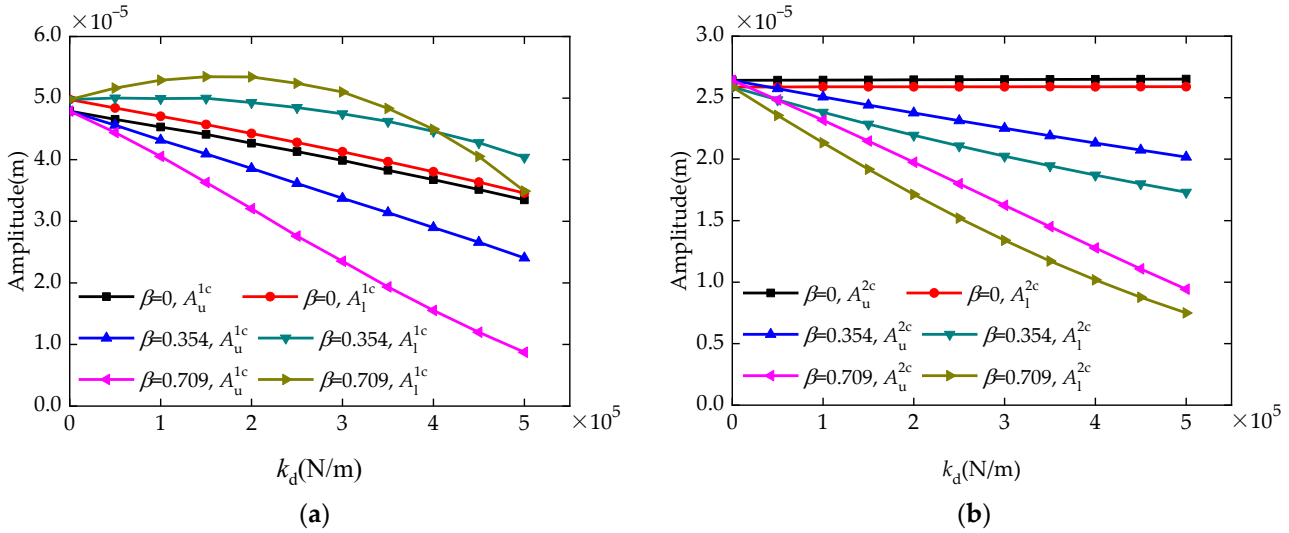


Figure 8. Under the critical speed, the FR's vibration amplitude curves at the positions of its upper and lower radial bearings along with k_d and β: (**a**) Amplitude curves below the ω_{1c}; (**b**) amplitude curves below the ω_{2c}.

In addition, as presented in Figure 8b, when $\beta = 0$, the change in motor stiffness k_d has no clear effect on the vibration amplitudes (A_u^{2c} and A_l^{2c}) under the position of the upper and lower radial bearings below the critical speed ω_{2c}. However, when $\beta \neq 0$, both A_u^{2c} and A_l^{2c} decrease with the increase in k_d and β, and their decreasing trends become more obvious as β increases. This means that when the axial spacing l_d is 0, the increase in the motor's UMP has no significant effect on the vibration amplitudes (A_u^{2c} and A_l^{2c}) at the radial bearing positions below the speed of ω_{2c}; however, both A_u^{2c} and A_l^{2c} decrease with the increase in l_d and UMP. This is noted because when l_d is 0, the change in UMP has no obvious effect on the supporting moment of FR and its second critical speed ω_{2c}. However, as UMP and l_d increase, the ω_{2c} of the FR declines, causing a reduction in the mass imbalance moment acting on the FR under the speed ω_{2c}. This leads to a decrease in the vibration amplitude at the position of the radial bearings under the speed ω_{2c}. Although as the UMP and l_d increase, the supporting moment of the FR decreases, which will lead to a rise in FR vibration amplitude. The reduction in vibration amplitude caused by the decrease in the mass unbalance moment at the speed ω_{2c} is more significant. Therefore, below the critical speed ω_{2c}, the vibration amplitudes of FR under its upper and lower radial bearing positions exhibit a decreasing trend. In the case where β is 0.355 and 0.709 and when $k_d = 2.5 \times 10^5$ N/m, A_u^{2c} decreases by 12.4% and 25.2%, respectively, and A_l^{2c} decreases by 18.6% and 33.8%, respectively. When $k_d = 5 \times 10^5$ N/m, A_u^{2c} decreases by 23.6% and 64.3%, respectively, and A_l^{2c} decreases by 33.1% and 71%, respectively. Thus, it can be seen that both the k_d and β produce an obvious effect on the vibration amplitudes

A_u^{2c} and A_l^{2c}, and the impact of these two factors on vibration amplitude at the lower radial bearing position is greater than that at the upper radial bearing position.

The above analysis reveals that the magnitude of the UMP and its acting location produce a significant impact on the vibration amplitude induced by the mass imbalance response of the FR under the critical speed. Reasonable motor parameter design can reduce the vibration amplitude of FR under its radial bearing positions at the critical speed, which helps the flywheel rotor to stably cross the critical speed range. However, the existence of UMP in the motor will reduce the overall support stiffness of the FR. When the flywheel energy storage system is subjected to external excitation, the running reliability of the active magnetically levitated flywheel rotor will be affected to some extent. Therefore, in the process of investigating the operational stability of the active magnetically levitated flywheel rotor under external excitation, the influence of the UMP in the motor should be considered.

5. Experiment

5.1. Experimental Setup

The experimental testing platform and its components are given in Figure 9. Figure 9a demonstrates the prototype of the active magnetically levitated flywheel energy storage system. The stator and controller of motor in this prototype are respectively shown in Figure 9b,c. The flywheel rotor adopts a vertical support structure, and both its radial and axial supports are equipped with active magnetic suspension bearings. Among them, the motor is the permanent magnet synchronous motor (PMSM) studied in this work, and it is driven and controlled by a frequency converter. This motor is located between the flywheel and the lower radial electromagnetic bearing, and the distance l_d between it and the mass center of FR is 0.111 m.

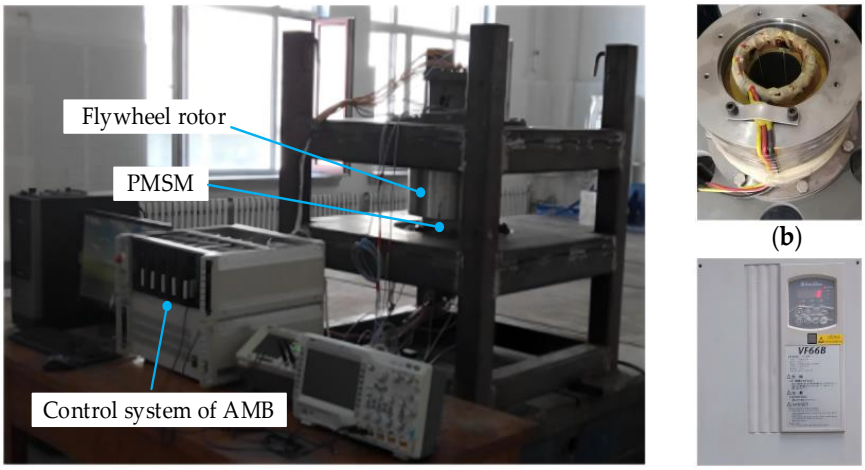


Figure 9. Experimental test platform: (**a**) Prototype of vertical active magnetically levitated flywheel energy storage system; (**b**) motor stator; (**c**) motor controller.

During the experimental testing process, the voltage signals from the eddy current displacement sensor of the radial active magnetically levitated bearing are collected using the PXI data acquisition system (sampling frequency is 3000 Hz). Converting the gathered signals based on the transformation relation between the voltage and displacement of the displacement sensor, the vibration amplitude signals of FR under the position of its radial bearings can be acquired. By conducting frequency domain analysis on these vibration signals, the vibration amplitude of FR at different speeds can be obtained; thus, the corresponding experimental vibration amplitude curve of the FR can be obtained.

5.2. Analysis of Theoretical and Experimental Test Results

The vibration amplitudes (A_u^e, A_l^e) of FR under the position of its upper and lower radial bearings obtained from the experimental tests are shown in Figure 10 as the red curve. The theoretical calculation results of the amplitude values (A_u^t, A_l^t) of FR without considering the UMP are shown in Figure 10 as the blue curve. Moreover, when considering the UMP in the motor, the corresponding theoretical results for the amplitudes (A_u^d, A_l^d) of FR under its upper and lower radial bearing positions are exhibited in Figure 10 as the pink curve.

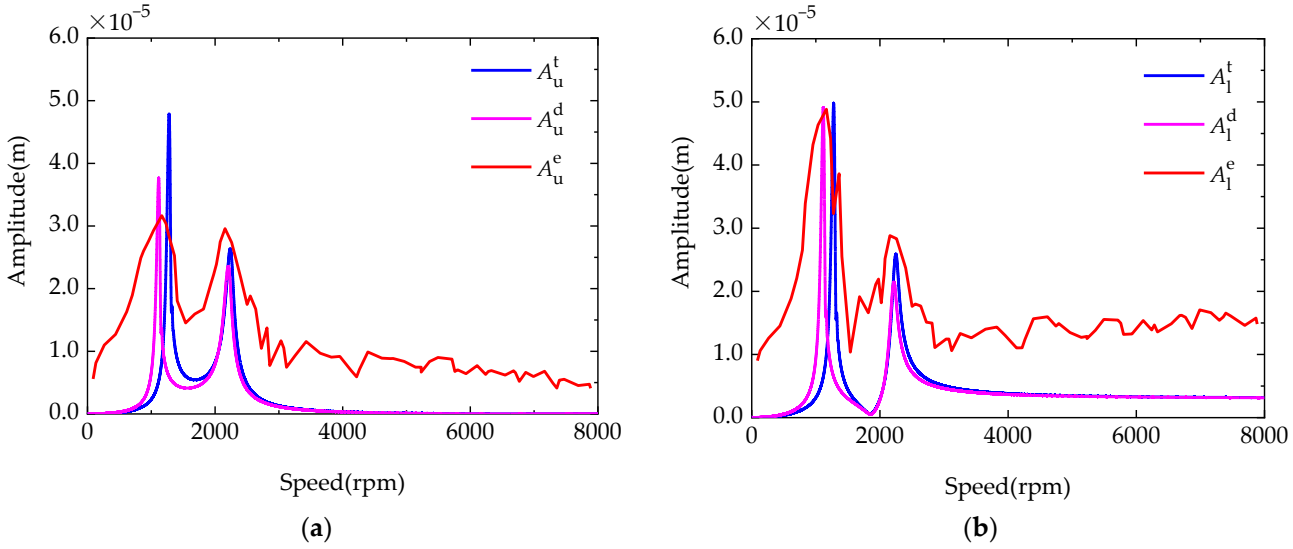


Figure 10. Theoretical calculation and experimental test results of the FR vibration amplitude under the position of its radial bearings: (**a**) Vibration amplitude at the position of the upper bearing; (**b**) vibration amplitude at the position of the lower bearing.

Figure 10 shows that the experimental as well as theoretical calculation vibration amplitude curves for FR under its radial bearing positions have a certain deviation in numerical values, but their overall trend of change has a good consistency. Among them, the measured results for the FR's first- and second-order critical rotational speeds are 1165 and 2155 rpm, respectively. When the UMP is not considered, the corresponding theoretical results are 1278 and 2238 rpm, respectively. These values are slightly larger than the experimental ones, and the relative deviations among them and the testing results are 9.7% and 3.8%, respectively. When considering the UMP of the motor, the corresponding theoretical results are 1115 and 2202 rpm, respectively, and the relative errors between them and the experimental results are 4.3% and 2.2%, respectively. In addition, in theoretical calculations, when considering the UMP, the first-order critical speed decreased by 163 rpm, while the second-order critical speed decreased by 36 rpm, indicating a significant difference in the changes between these two critical speeds. This is mainly because the factors affecting the first and second critical speeds are different. Among them, the first critical speed is closely related to the mass of the FR and its radial support force, while the second critical speed is related to its equatorial moment of inertia and support torque.

From this, it can be evident that when considering the UMP in the motor, the relative error among their calculated and tested results is smaller. Furthermore, when taking into account the UMP, the calculated vibration amplitudes are more closer to their experimental results. This verifies the correctness of the theoretical model established in this paper and the validity of the conclusions obtained from this investigation. In addition, there are some deviations between the theoretical model and the experimental system that ignore the three-dimensional effects of the magnetic field in motor and the stiffness of the foundation

frame. This will lead to some errors, and in future research, the theoretical model can be further improved to reduce errors.

6. Conclusions

This paper primarily investigated the influence of the motor UMP on the vibration characteristics of the FR in an active magnetically suspended flywheel energy storage system. The variation rules for the UMP caused by rotor eccentricity in a permanent magnet synchronous motor (PMSM) adapted to FESS were analyzed using the finite element method. On this basis, a dynamic model of the magnetically suspended rigid flywheel rotor taking into account the UMP was constructed, and the impact of the magnitude of this motor UMP and its acting location on the vibration properties of FR was explored. Furthermore, the correctness of the theoretical results was verified using experiments. The conclusions obtained from this investigation were as follows:

1. The unbalanced magnetic pull (UMP) in the PMSM increased as the rotor eccentricity increased. The magnitude of this UMP fluctuated with the increase in the rotor rotation angle; however, this fluctuation amplitude was relatively small compared to the value of the motor UMP. Overall, the UMP presented a linear increase trend with the increase in rotor eccentricity.
2. The first- and second-order critical rotational speeds of the active magnetic suspension flywheel rotor both decreased as the motor UMP and its axial position offset ratio β increased. When the motor stiffness k_d was 2.5×10^5 N/m and the offset ratios β were 0.354 and 0.709, the first critical speed decreased by 14.6% and 17.5%, respectively, and the second critical speed decreased by 1.4% and 4.8%, respectively. Moreover, the size of the motor UMP and its acting location also had a significant effect on the vibration amplitude induced by the mass imbalance response of the FR.
3. When considering the UMP in the motor, the calculated results for the vibration characteristics of the active magnetic suspension flywheel rotor were more similar to the measured ones, which validated the correctness of the established theoretical model and the conclusions obtained in this paper. During the analysis of the rotor vibration characteristics of an active magnetically suspended flywheel energy storage system, the impact of the motor UMP should be taken into account.

Author Contributions: Conceptualization, L.W.; methodology, L.W.; software, L.W.; validation, L.W., T.L. and Z.R.; investigation, L.W.; resources, T.L. and Z.R.; data curation, L.W.; writing—original draft preparation, L.W.; writing—review and editing, L.W.; visualization, L.W.; supervision, T.L. and Z.R. All authors have read and agreed to the published version of the manuscript.

Funding: This work is supported by the National High-tech Research and Development Program of China (Grant No. 2013AA050802) and the Fundamental Research Special Funds for the Central Universities of Harbin Engineering University (Grant No. HEUCFZ1024).

Institutional Review Board Statement: Not applicable.

Informed Consent Statement: Not applicable.

Data Availability Statement: The original contributions presented in this study are included in the article. Further inquiries can be directed to the corresponding author.

Conflicts of Interest: The authors declare no conflicts of interest.

References

1. Mahmoud, M.; Ramadan, M.; Olabi, A.G.; Pullen, K.; Naher, S. A review of mechanical energy storage systems combined with wind and solar applications. *Energy Convers. Manag.* **2020**, *210*, 112670. [CrossRef]
2. Qi, Z.N.; Zhang, Y.; Yu, S.Y.; Fu, Z.J. Design and Analysis of the Multilayer Sleeve Structure for the Rotor Eddy Current Loss Reduction of a High-Speed Permanent Magnet Motor for Flywheel Energy Storage System. *IEEE Trans. Transp. Electrif.* **2025**, *11*, 11398–11409. [CrossRef]
3. Tziovani, L.; Hadjidemetriou, L.; Charalampous, C.; Tziakouri, M.; Timotheou, S.; Kyriakides, E. Energy Management and Control of a Flywheel Storage System for Peak Shaving Applications. *IEEE Trans. Smart Grid* **2021**, *12*, 4195–4207. [CrossRef]
4. Soomro, A.; Amiryar, M.E.; Pullen, K.R.; Nankoo, D. Comparison of Performance and Controlling Schemes of Synchronous and Induction Machines Used in Flywheel Energy Storage Systems. In Proceedings of the 3rd Annual Conference in Energy Storage and Its Applications (3rd CDT-ESA-AC), Sheffield, UK, 11–12 September 2018.
5. Yan, Z.G.; Wu, S.P.; Huang, M.P.; Zhang, W.; Zhang, M.; Zhang, P.L. A Stator-PM Counter-Rotating Dual-Rotor High-Speed Electrical Machine for Flywheel Energy Storage System. *IEEE Trans. Ind. Electron.* **2025**, *73*, 4506–4517.
6. Hüner, E. A New Multi-Axial Flux Pm Motor-Generator System for Flywheel Energy Storage. *Appl. Sci.* **2025**, *15*, 2524. [CrossRef]
7. Ye, C.Y.; Yu, D.Z.; Liu, K.F.; Dai, Y.Z.H.; Deng, C.; Yang, J.T.; Zhang, J.P. Research of a Stator PM Excitation Solid Rotor Machine for Flywheel Energy Storage System. *IEEE Trans. Ind. Electron.* **2022**, *69*, 12140–12151. [CrossRef]
8. Zhou, Y.; Bao, X.H.; Di, C.; Wang, L. Analysis of dynamic unbalanced magnetic pull in induction motor with dynamic eccentricity during starting period. *IEEE Trans. Magn.* **2016**, *52*, 8202604. [CrossRef]
9. Zhang, A.; Bai, Y.; Yang, B.; Li, H. Analysis of Nonlinear Vibration in Permanent Magnet Synchronous Motors under Unbalanced Magnetic Pull. *Appl. Sci.* **2018**, *8*, 113. [CrossRef]
10. Gruber, W.; Hinterdorfer, T.; Sima, H.; Schulz, A.; Wassermann, J. Comparison of different motor-generator sets for long term storage flywheels. In Proceedings of the IEEE International Symposium on Power Electronics, Electrical Drives, Automation and Motion (SPEEDAM), Ischia, Italy, 18–20 June 2014.
11. Sun, X.D.; Su, B.K.; Wang, S.H.; Yang, Z.B.; Lei, G.; Zhu, J.G.; Guo, Y.G. Performance Analysis of Suspension Force and Torque in an IBPMSM with V-Shaped PMs for Flywheel Batteries. *IEEE Trans. Magn.* **2018**, *54*, 8105504. [CrossRef]
12. Liu, K.; Yin, M.; Hua, W.; Ma, Z.Q.; Lin, M.Y.; Kong, Y. Design and Optimization of an External Rotor Ironless BLDCM Used in a Flywheel Energy Storage System. *IEEE Trans. Magn.* **2018**, *54*, 8109105. [CrossRef]
13. Sun, M.X.; Xu, Y.L.; Han, K. Structure and Optimization Design of Cup Winding Permanent Magnet Synchronous Machine in Flywheel Energy Storage System. *IEEE Trans. Magn.* **2023**, *59*, 8100805. [CrossRef]
14. Sun, M.X.; Xu, Y.L.; Zhang, W.J. Multiphysics Analysis of Flywheel Energy Storage System Based on Cup Winding Permanent Magnet Synchronous Machine. *IEEE Trans. Energy Convers.* **2023**, *38*, 2684–2694. [CrossRef]
15. Sun, M.X.; Xu, Y.L.; Li, G.S. Analysis of No-Load Operation of Cup Winding Permanent Magnet Synchronous Machine in Flywheel Energy Storage Application. *IEEE/ASME Trans. Mechatron.* **2024**, *29*, 3739–3749. [CrossRef]
16. Wang, G.J.; Wang, P.; Wang, X.Y. Equivalent Magnetic Circuit Reluctance Optimization for Rotor Loss Reduction in Permanent Magnet Synchronous Motor for UPS-FESS. *IEEE Access* **2020**, *8*, 107593–107600. [CrossRef]
17. Chen, Y.G.; Zang, B.Q.; Wang, H.T.; Liu, H.X.; Li, H.R. Research on Composite Rotor of 200kW Flywheel Energy Storage System High Speed Permanent Magnet Synchronous Motor for UPS. In Proceedings of the 24th International Conference on Electrical Machines and Systems (ICEMS), Gyeongju, Republic of Korea, 31 October–3 November 2021.
18. Li, Y.W.; Zhu, C.S.; Wu, L.J.; Zheng, Y.T. Multi-Objective Optimal Design of High-Speed Surface-Mounted Permanent Magnet Synchronous Motor for Magnetically Levitated Flywheel Energy Storage System. *IEEE Trans. Magn.* **2019**, *55*, 8202708. [CrossRef]
19. Jiang, X.J.; Zhang, L.; Li, F.W.; Zhao, Z.H. Design and Analysis of a Highly Reliable Permanent Magnet Synchronous Machine for Flywheel Energy Storage. *Machines* **2024**, *12*, 655. [CrossRef]
20. Dagnaes-Hansen, N.A.; Santos, I.F. Magnetically suspended flywheel in gimbal mount-Nonlinear modelling and simulation. *J. Sound Vib.* **2018**, *432*, 327–350. [CrossRef]
21. Yang, Y.; Liu, C.N.; Chen, L.; Zhang, X.L. Phase deviation of semi-active suspension control and its compensation with inertial suspension. *Acta Mech. Sin.* **2024**, *40*, 523367. [CrossRef]
22. Li, J.T.; Liu, Z.J.; Nay, L.H.A. Effect of Radial Magnetic Forces in Permanent Magnet Motors With Rotor Eccentricity. *IEEE Trans. Magn.* **2007**, *43*, 2525–2527. [CrossRef]
23. Song, Y.X.; Liu, Z.Y.; Hou, R.J.; Gao, H.J.; Huang, B.; Wu, D.Z.; Liu, J.T. Research on electromagnetic and vibration characteristics of dynamic eccentric PMSM based on signal demodulation. *J. Sound Vib.* **2022**, *541*, 117320. [CrossRef]
24. Zhang, H.S.; Liu, Y.B.; Teng, W.; Song, S.Y.; Wang, Y.J. Dynamic characteristics analysis of energy storage flywheel motor rotor with air-gap eccentricity fault. *J. Energy Storage* **2024**, *89*, 111684. [CrossRef]
25. Xu, X.P.; Liu, Y.; Han, Q.K. A universal dynamic model and solution scheme for the electrical rotor system with wide range of eccentricity. *Int. J. Non-Linear Mech.* **2023**, *152*, 104402. [CrossRef]

26. Liu, F.; Xiang, C.L.; Liu, H.; Chen, X.; Feng, F.Z.; Cong, H.; Yu, K.L. Model and experimental verification of a four degrees-of-freedom rotor considering combined eccentricity and electromagnetic effects. *Mech. Syst. Signal Process.* **2022**, *169*, 108740. [CrossRef]
27. Hao, J.; Yao, Z.H.; Li, C.Y.; Song, W.J.; Miao, H.H.; Xu, M.T.; Liu, Z.D. Dynamic characteristics analysis of asynchronous motorized spindle considering combined unbalanced magnetic pull and nonlinear bearing restoring force effects. *Mech. Syst. Signal Process.* **2023**, *185*, 109807. [CrossRef]
28. Dai, W.; Zhang, H.; Halim, D.; Yang, J.; Xu, Z.Y.; Li, J. Rotordynamic Analysis of a Permanent Magnet Synchronous Motor Considering Nonlinear Unbalanced Magnetic Pull. In Proceedings of the 22nd International Conference on Electrical Machines and Systems (ICEMS), Harbin, China, 11–14 August 2019.
29. Michon, M.; Atallah, K.; Johnstone, G. Effects of unbalanced magnetic pull in large permanent magnet machines. In Proceedings of the IEEE Energy Conversion Congress and Exposition (ECCE), Pittsburgh, PA, USA, 14–18 September 2014.
30. Feng, W.; Zhang, K.; Liu, B.G.; Sun, W.F.; Cai, S.J. Dynamic modeling and vibration response analysis of a synchronous motorized spindle with inclined eccentricity. *J. Vib. Control* **2022**, *28*, 2950–2964.
31. Wang, L.; Li, T.L.; Ren, Z.Y. The Influence of Axial Bearing Position of Active Magnetic Suspension Flywheel Energy Storage System on Vibration Characteristics of Flywheel Rotor. *Actuators* **2025**, *14*, 290. [CrossRef]

Disclaimer/Publisher's Note: The statements, opinions and data contained in all publications are solely those of the individual author(s) and contributor(s) and not of MDPI and/or the editor(s). MDPI and/or the editor(s) disclaim responsibility for any injury to people or property resulting from any ideas, methods, instructions or products referred to in the content.